Electronic Supplementary Material (ESI) for Journal of Materials Chemistry A.

Supporting Information

Hot Carrier Relaxation Dynamics in Non-Stoichiometric CdSe Quantum Dots: Computational Insights

Shriya Gumber,[1,7] Omolola Eniodunmo,[2,7] Sergei Ivanov,[3] Svetlana Kilina,[2] Oleg V. Prezhdo,[1,4] Dibyajyoti Ghosh,[5,6]*, and Sergei Tretiak[3,7]*

[1]*Department of Chemistry, University of Southern California, Los Angeles, California 90089, USA*

[2]*Dept. Chemistry and Biochemistry, North Dakota State University, Fargo, North Dakota 58108, US,*

[3]*Center for Integrated Nanotechnologies, Los Alamos National Laboratory, Los Alamos, NM, 87545, USA*

[4]*Department of Physics and Astronomy, University of Southern California, Los Angeles, California 90089, USA*

[5]*Department of Chemistry, Indian Institute of Technology, Delhi, Hauz Khas, New Delhi-110016, India*

[6]*Department of Materials Science and Engineering (DMSE), Indian Institute of Technology, Delhi, Hauz Khas, New Delhi-110016, India*

[7]*Theoretical Division, Los Alamos National Laboratory, Los Alamos, NM, 87545, USA*

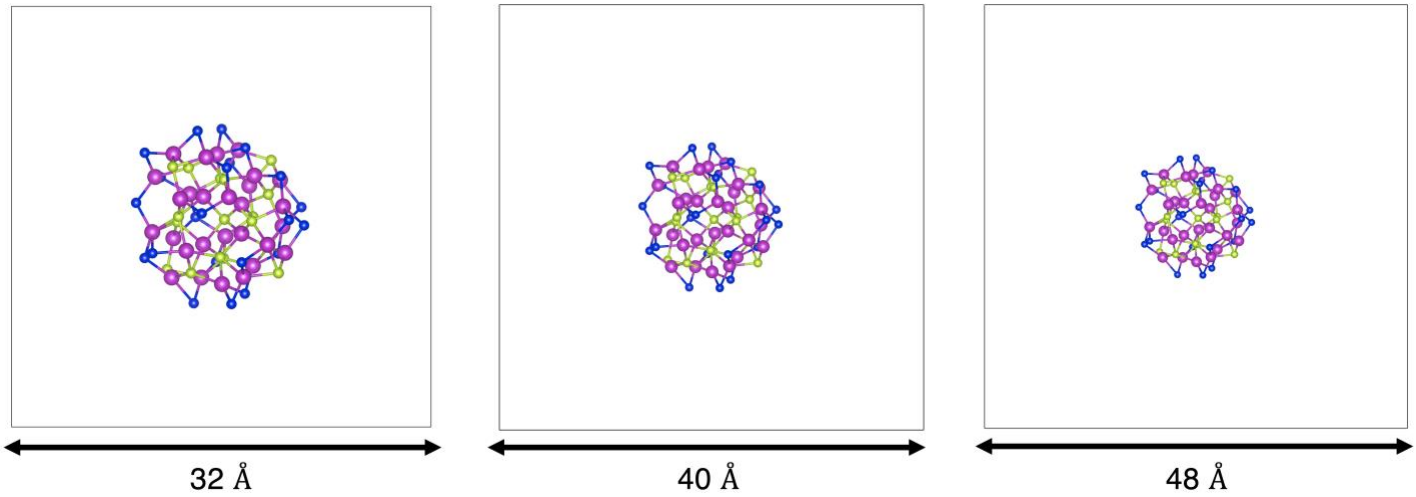

Figure S1. The non-stoichiometric Cd-rich quantum dot $Cd_{28}Se_{17}Cl_{22}$ contained in cubic simulation cell of different lattice vector lengths indicated below each box. Atomic colour scheme: Pink: Cd, Green: Se, Blue: Cl.

Table S1. The lattice vector length of the cubic simulation cell containing QDs used for all calculations in this paper. The smallest distance between a QD and its replica in x, y, and z direction is also listed.

		$Cd_{33}Se_{33}$	$Cd_{28}Se_{17}F_{22}$	$Cd_{28}Se_{17}Cl_{22}$	$Cd_{17}Se_{28}H_{22}$	$Cd_{17}Se_{28}Na_{22}$	$Cd_{17}Se_{28}K_{22}$
Lattice vector length (Å)		28.0	32.0	32.0	34.6	32.0	32.0
Distance between QDs (Å)	x	16.2	20.0	19.5	21.6	20.5	19.8
	y	14.5	20.8	19.7	22.0	19.4	18.7
	z	16.2	20.7	20.0	21.9	19.2	20.2

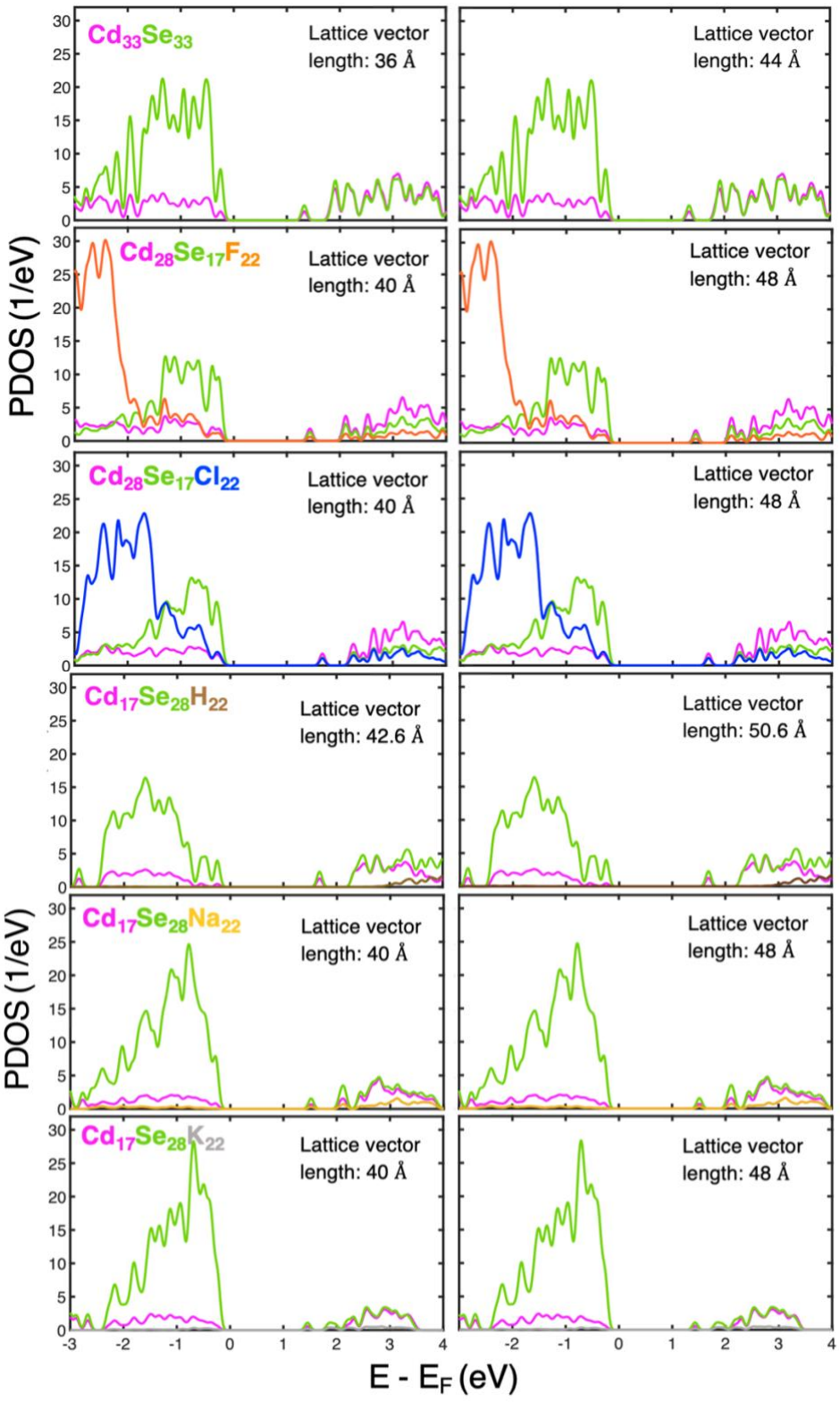

Figure S2. PDOS separated into contribution from atomic orbitals for all QDs in larger cubic simulation cell than that plotted in figure 2 in main paper. The PDOS does not change on increasing the vacuum around QDs suggesting that the simulation cell dimension in figure 2 is sufficient to avoid QD interaction with its replica.

Table S2. Comparison of band-gap and the projection of HOMO and LUMO over Cd, Se, and ligand (L) atomic orbitals for QDs in cubic simulation cells of varied lattice vector lengths. If $|c_{\alpha,i}|^2$ represents the magnitude of projection of i^{th} KS state over α atomic orbital, then the projection of HOMO (or LUMO) over Cd (or Se or L) atomic orbital is obtained by this sum: $\sum_{Cd} |c_{Cd,HOMO}|^2$.

			HOMO			LUMO		
	a (Å)	Band-gap	Cd	Se	L	Cd	Se	L
$Cd_{33}Se_{33}$	28	1.59	0.097	0.484	-	0.183	0.279	-
	36	1.58	0.098	0.482	-	0.183	0.279	-
	44	1.58	0.098	0.484	-	0.183	0.277	-
$Cd_{28}Se_{17}F_{22}$	32	1.69	0.097	0.456	0.056	0.253	0.170	0.078
	40	1.69	0.099	0.454	0.056	0.252	0.169	0.078
	48	1.69	0.099	0.455	0.057	0.252	0.170	0.078
$Cd_{28}Se_{17}Cl_{22}$	32	1.91	0.097	0.424	0.098	0.236	0.150	0.136
	40	1.91	0.097	0.424	0.098	0.237	0.150	0.136
	48	1.91	0.097	0.424	0.098	0.237	0.150	0.136
$Cd_{17}Se_{28}H_{22}$	34.6	1.93	0.061	0.499	0.002	0.162	0.297	0.004
	42.6	1.93	0.061	0.499	0.002	0.162	0.297	0.004
	50.6	1.93	0.061	0.499	0.002	0.161	0.296	0.004
$Cd_{17}Se_{28}Na_{22}$	32	1.77	0.049	0.492	0.009	0.095	0.197	0.041
	40	1.77	0.048	0.491	0.009	0.095	0.197	0.041
	48	1.77	0.048	0.490	0.009	0.095	0.197	0.041
$Cd_{17}Se_{28}K_{22}$	32	1.69	0.042	0.480	0.011	0.079	0.145	0.027
	40	1.68	0.040	0.480	0.011	0.079	0.145	0.027
	48	1.68	0.040	0.475	0.011	0.079	0.146	0.027

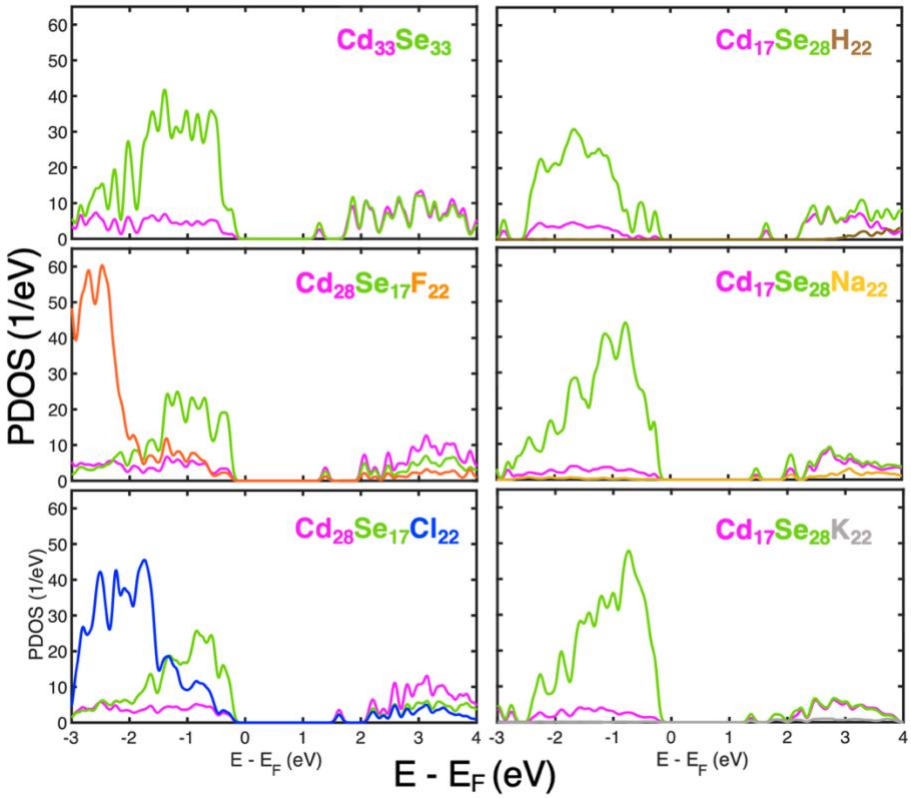

Figure S3. Projected density of states (PDOS) separated into contributions from atomic orbitals for stoichiometric and non-stoichiometric systems under investigation. Spin orbit coupling is included to obtain these results. The fermi energy level is set to 0.

Table S3. Comparison of band-gap and the projection of HOMO and LUMO over Cd, Se, and ligand (L) atomic orbitals for QDs in with and without spin-orbit coupling. If $|c_{\alpha,i}|^2$ represents the magnitude of projection of i^{th} KS state over α atomic orbital, then the projection of HOMO (or LUMO) over Cd (or Se or L) atomic orbital is obtained by this sum: $\sum_{Cd} |c_{Cd,HOMO}|^2$.

			HOMO			LUMO		
		Band-gap	Cd	Se	L	Cd	Se	L
$Cd_{33}Se_{33}$	w/o SOC	1.59	0.097	0.484	-	0.183	0.279	-
	w SOC	1.51	0.091	0.483	-	0.183	0.277	-
$Cd_{28}Se_{17}F_{22}$	w/o SOC	1.69	0.097	0.456	0.056	0.253	0.170	0.078
	w SOC	1.66	0.099	0.448	0.057	0.253	0.169	0.078
$Cd_{28}Se_{17}Cl_{22}$	w/o SOC	1.91	0.097	0.424	0.098	0.236	0.150	0.136
	w SOC	1.88	0.099	0.418	0.099	0.236	0.150	0.136
$Cd_{17}Se_{28}H_{22}$	w/o SOC	1.93	0.061	0.499	0.002	0.162	0.297	0.004
	w SOC	1.92	0.063	0.497	0.003	0.162	0.297	0.004
$Cd_{17}Se_{28}Na_{22}$	w/o SOC	1.77	0.049	0.492	0.009	0.095	0.197	0.041
	w SOC	1.75	0.052	0.490	0.008	0.096	0.197	0.041
$Cd_{17}Se_{28}K_{22}$	w/o SOC	1.69	0.042	0.480	0.011	0.079	0.145	0.027
	w SOC	1.64	0.047	0.474	0.011	0.079	0.144	0.027

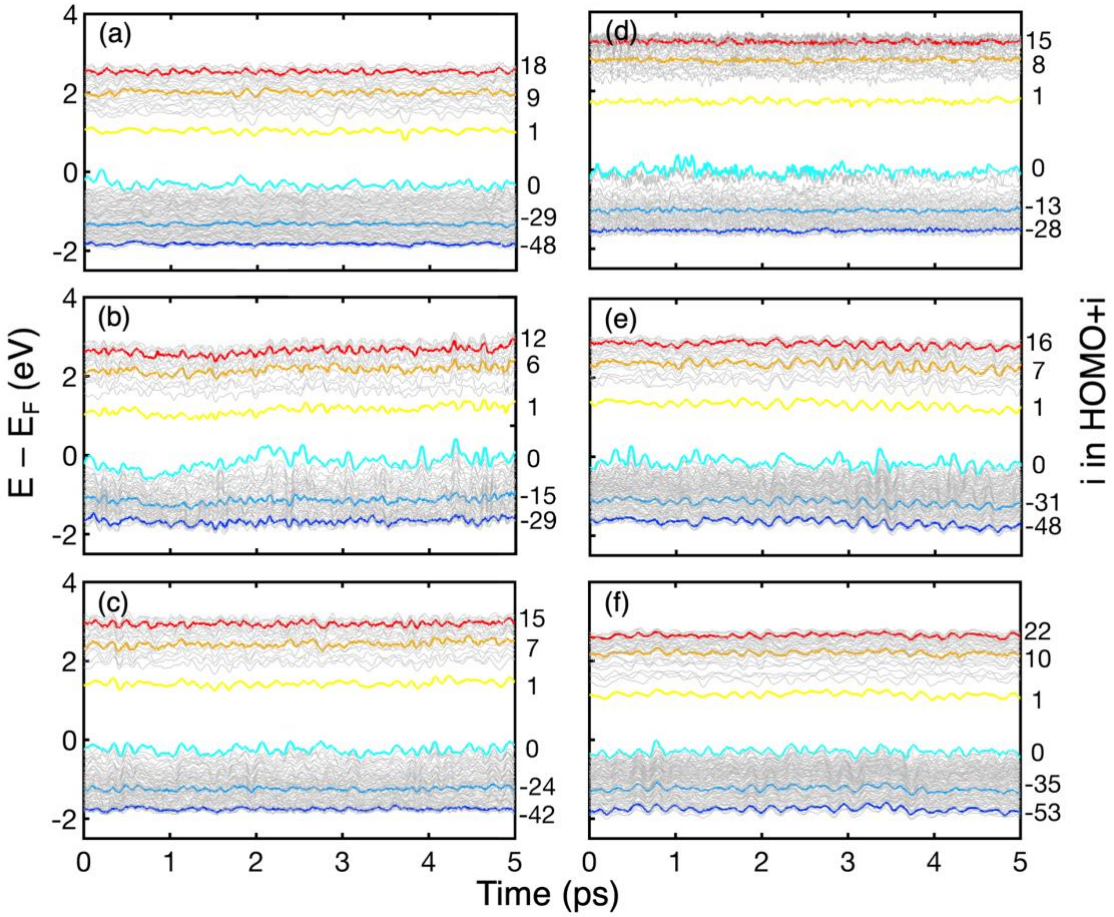

Figure S4. Time evolution of electronic energy states in stoichiometric (a) $Cd_{33}Se_{33}$ and non-stoichiometric: Cd-rich (b) $Cd_{28}Se_{17}F_{22}$, (c) $Cd_{28}Se_{17}Cl_{22}$, and Se-rich, (d) $Cd_{17}Se_{28}H_{22}$, (e) $Cd_{17}Se_{28}Na_{22}$, (f) $Cd_{17}Se_{28}K_{22}$ quantum dots. The fermi energy level is set to 0. The light blue colored state with $i = 0$ and yellow colored state with $i = 1$ represents the HOMO and LUMO, respectively. The orange and red colored electronic energy states lie at an average of 1 eV and 1.5 eV, respectively from the LUMO. Similarly, the navy blue and royal blue colored electronic energy states lie at an average of 1 eV and 1.5 eV, respectively from the HOMO. These states at 1 eV and 1.5 eV from the LUMO (HOMO) are considered as initially excited states for electron (hole) relaxation dynamics.

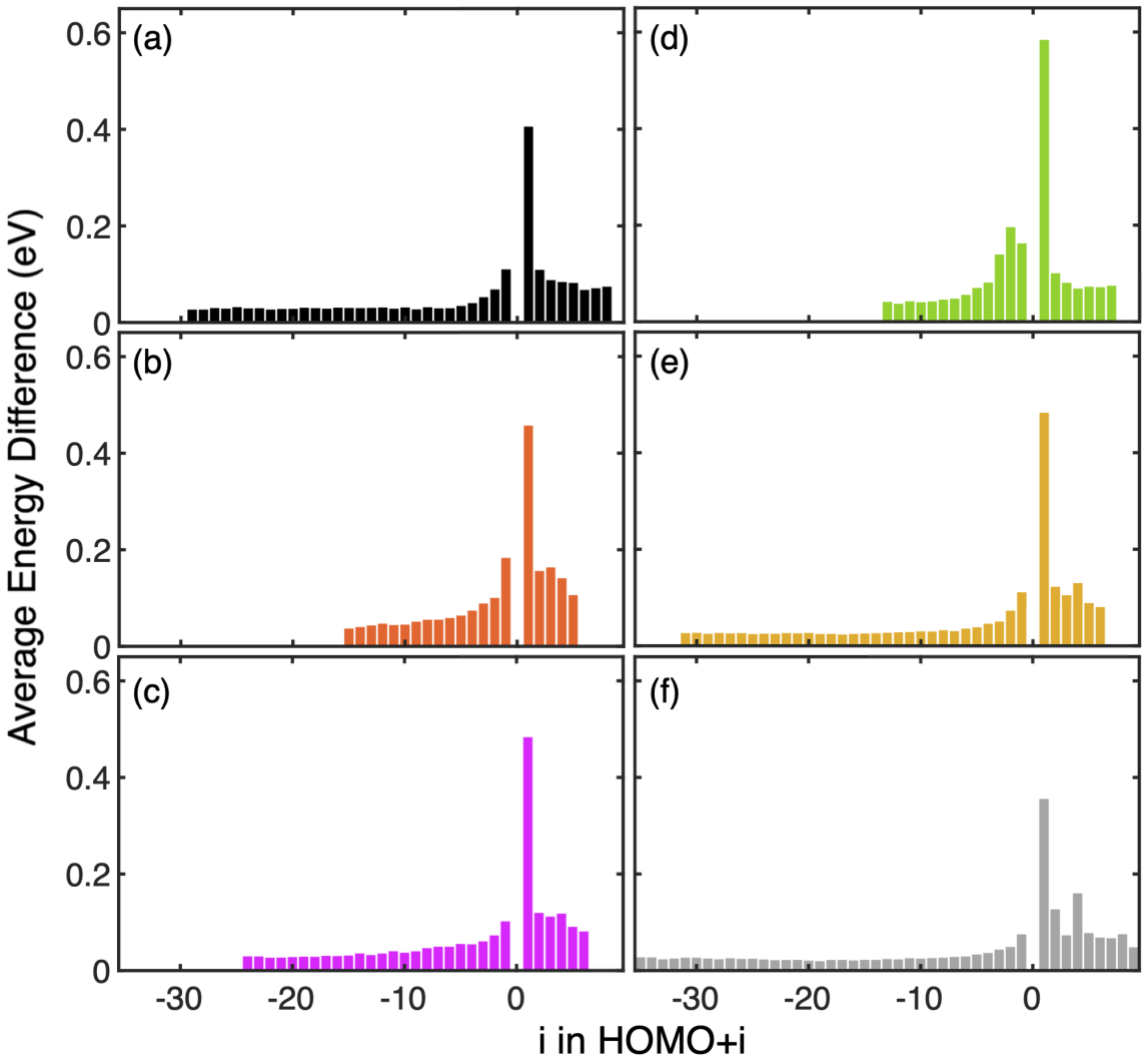

Figure S5. The energy difference between the Kohn-Sham orbitals averaged over the 5 ps AIMD trajectory for (a) $Cd_{33}Se_{33}$, (b) $Cd_{28}Se_{17}F_{22}$, (c) $Cd_{28}Se_{17}Cl_{22}$, (d) $Cd_{17}Se_{28}H_{22}$, (e) $Cd_{17}Se_{28}Na_{22}$ and (f) $Cd_{17}Se_{28}K_{22}$ quantum dots. We consider only the orbitals within the energy range from LUMO to 1 eV higher and from HOMO to 1 eV lower energy. HOMO-LUMO energy gap is not shown here as we do not model the charge recombination across the band gap in our study for this paper.

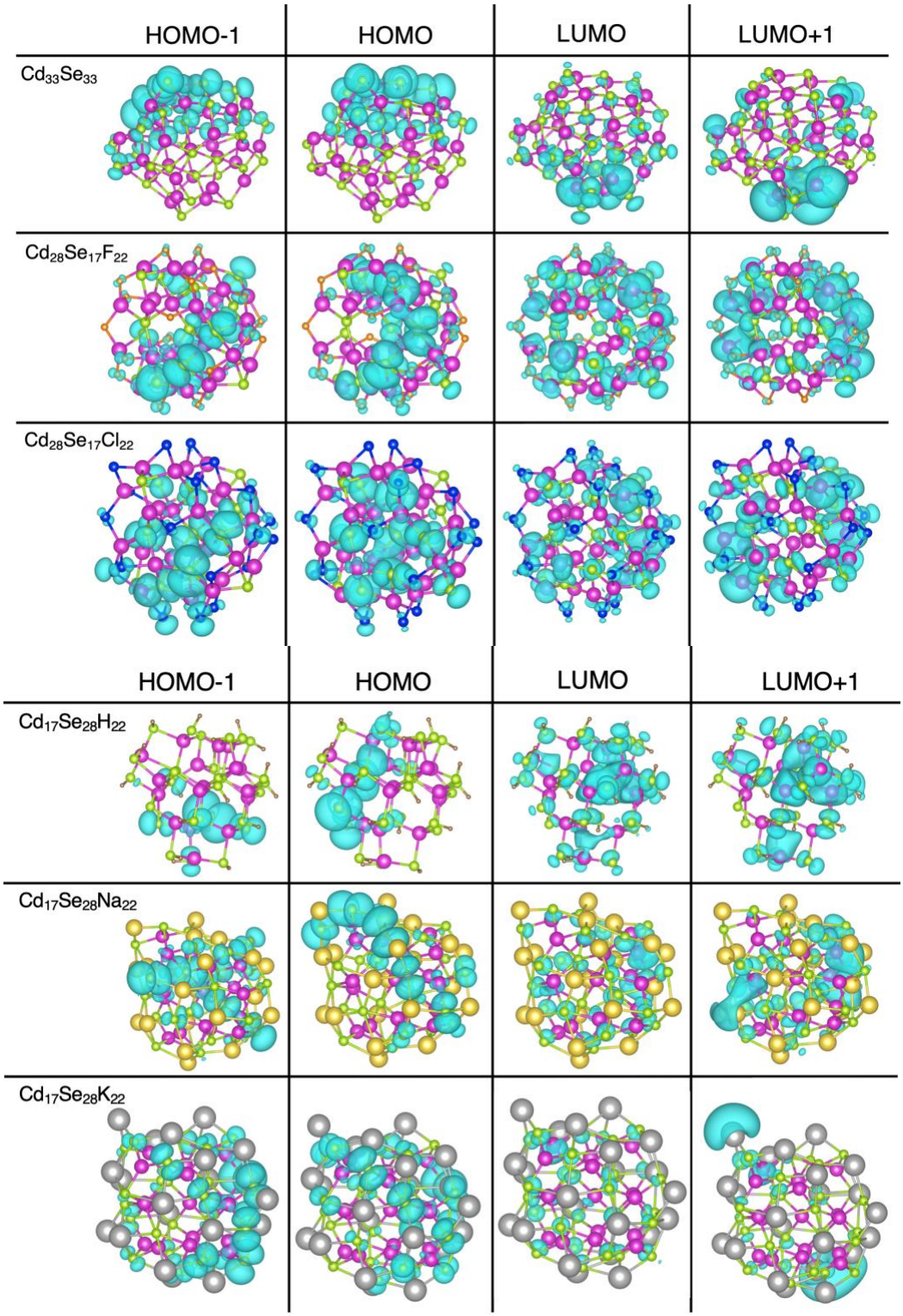

Figure S6. The charge density plots of first two orbitals in valence band (HOMO-1, HOMO) and conduction band (LUMO, LUMO+1) in turquoise colour calculated at isosurface level of 0.0005 a_o^{-3} (where a_o is the Bohr radius), for all QDs under investigation. Atom label: Se- green, Cd- pink, F-orange, Cl-blue, H-brown, Na-yellow, K-gray.

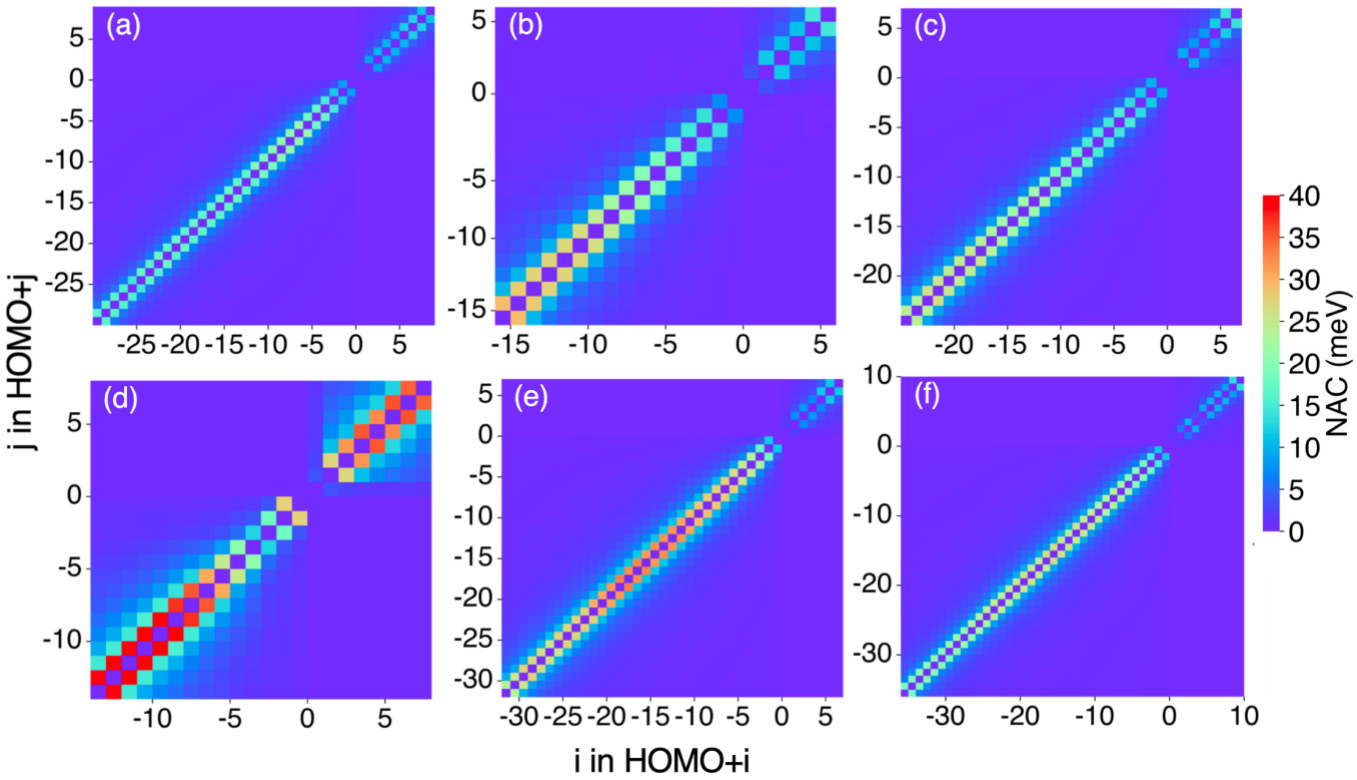

Figure S7. Non-adiabatic coupling (NAC) in the form of a heatmap, for a) stoichiometric, and (b) F, (c) Cl, (d) H, (e) Na and (f) K ligated non-stoichiometric quantum dots. The heatmap scale is shown on the right. The maps are symmetric since the coupling of Kohn Sham (KS) orbital i with orbital j is equal to the coupling of KS orbital j with i. The purple diagonal elements in the middle represent the coupling of an orbital element with itself and hence it is zero. The axis scale of each plot is such as to include all orbitals within the range: (i) LUMO to 1 eV higher, and (ii) HOMO to 1 eV lower. Coupling magnitude when KS orbitals differ by more than one is close to zero.

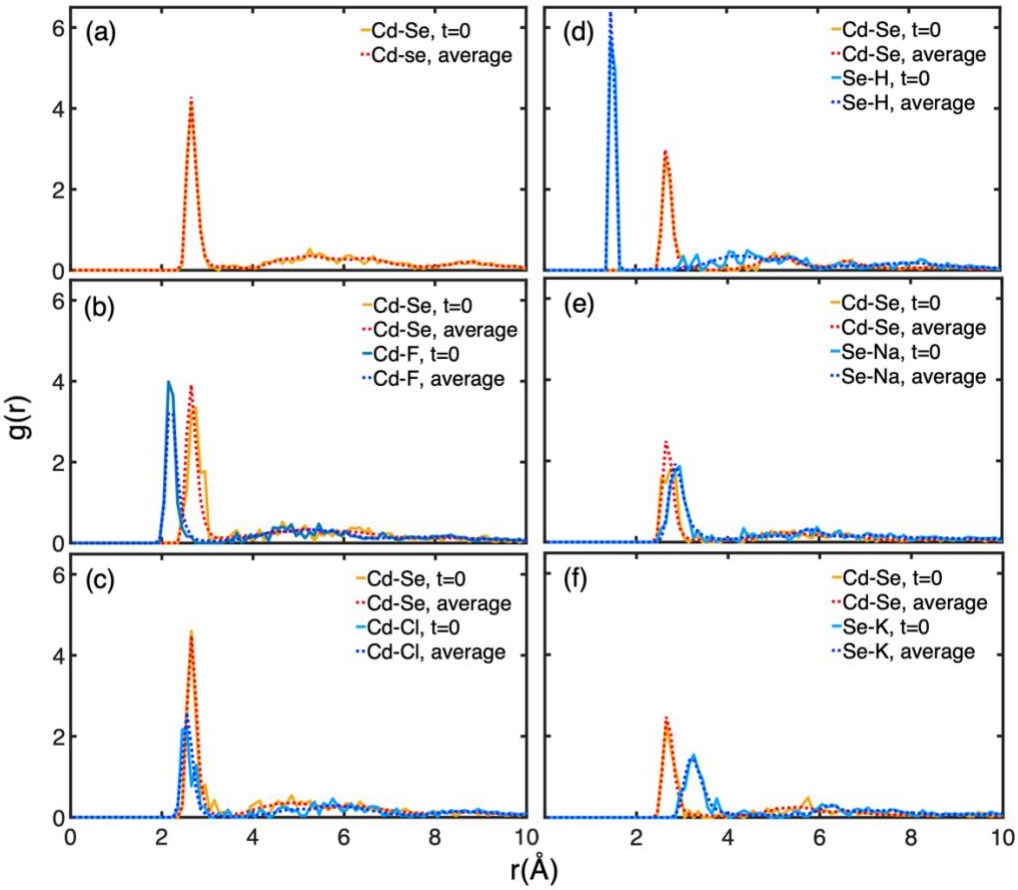

Figure S8. Comparison of the radial distribution function (g(r)) of Cd-Se bond (shown in red and yellow) and Cd/Se-ligand bond (shown in light and dark blue) in static structure at $t = 0$ and the averaged structure over 5 picoseconds AIMD trajectory for a) $Cd_{33}Se_{33}$, (b) $Cd_{28}Se_{17}F_{22}$, (c) $Cd_{28}Se_{17}Cl_{22}$, (d) $Cd_{17}Se_{28}H_{22}$, (e) $Cd_{17}Se_{28}Na_{22}$, and (f) $Cd_{17}Se_{28}K_{22}$ quantum dots. Due to the small size and large coordination number of F and Na ligands, the surface Cd/Se atoms of corresponding nanostructures are more dynamic compared to others. Overall, g(r) insignificantly deviates from the static one during AIMD dynamics at room temperature, ensuring the stability of all nanostructures.

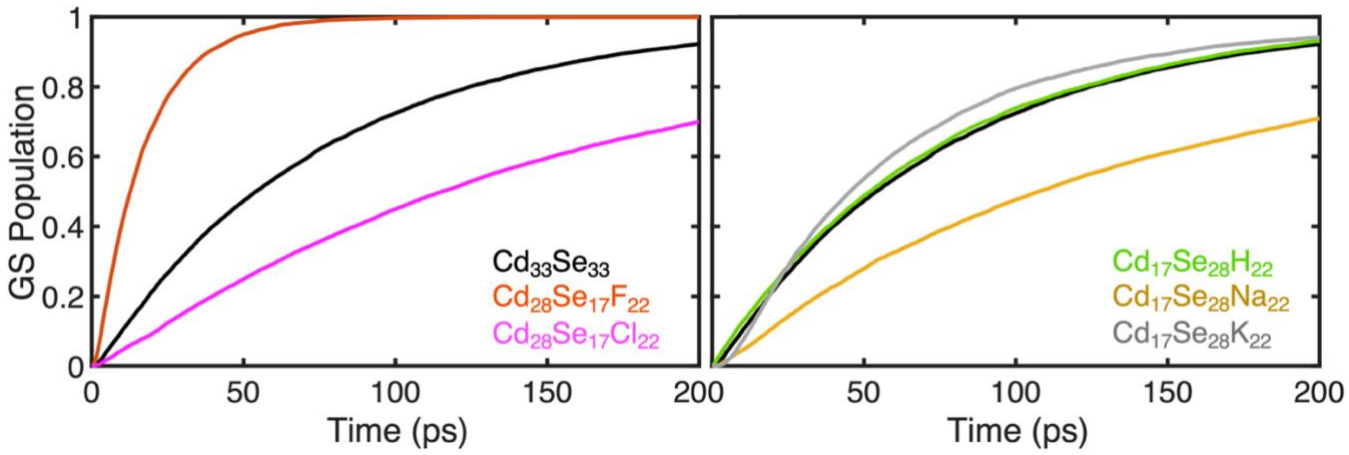

Figure S9. The GS population evolution for the energy dissipation for electron relaxation starting at 1 eV higher initial state for Cd-rich QDs (left) and Se-rich QDs (right). Corresponding energy dissipation is shown in Figure 4 in main paper.

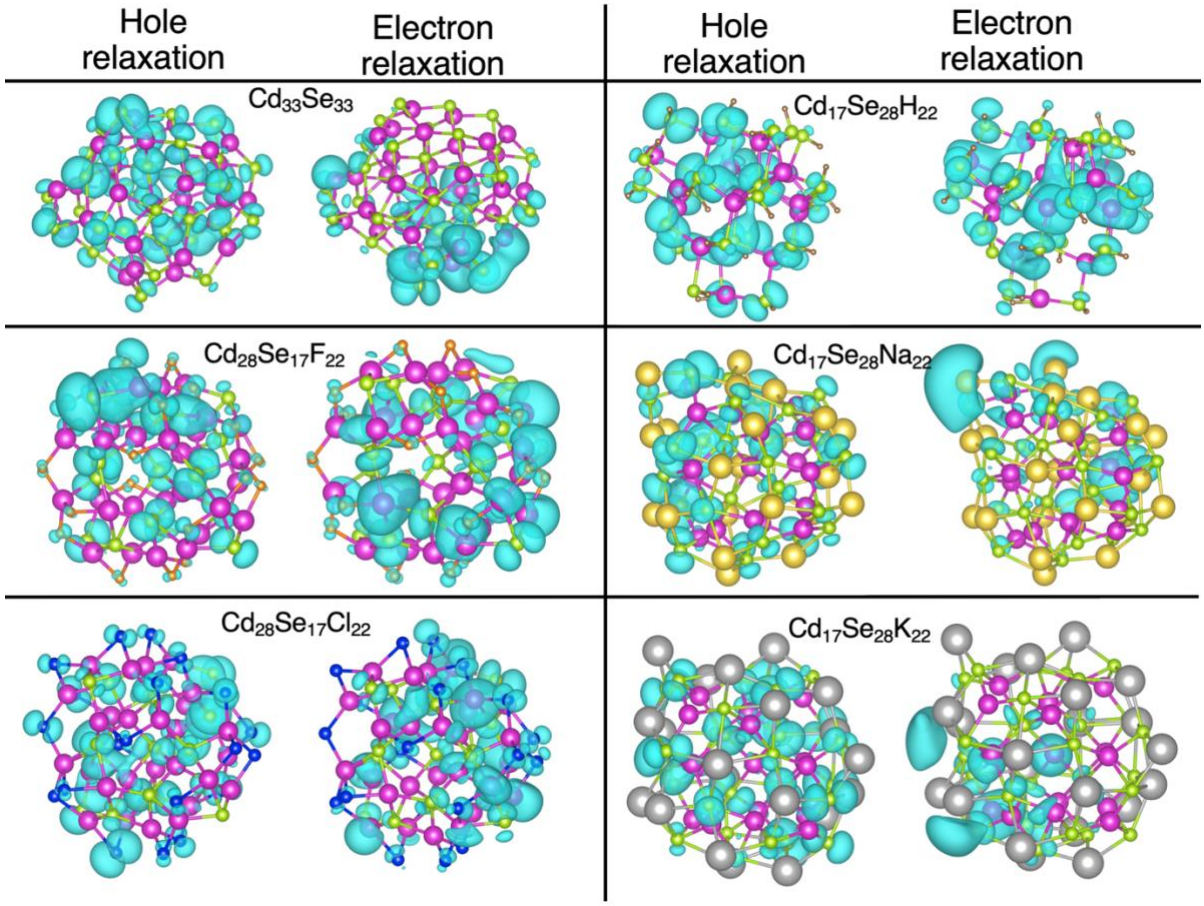

Figure S10. The charge density plots (in turquoise color) of the initial Kohn Sham orbitals for electron and hole relaxation starting at 1 eV energy. The isosurface level of 0.0005 a_o^{-3} (where a_o is the Bohr radius) is used for all plots). Atom label: Se- green, Cd- pink, F-orange, Cl-blue, H-brown, Na-yellow, K-gray.

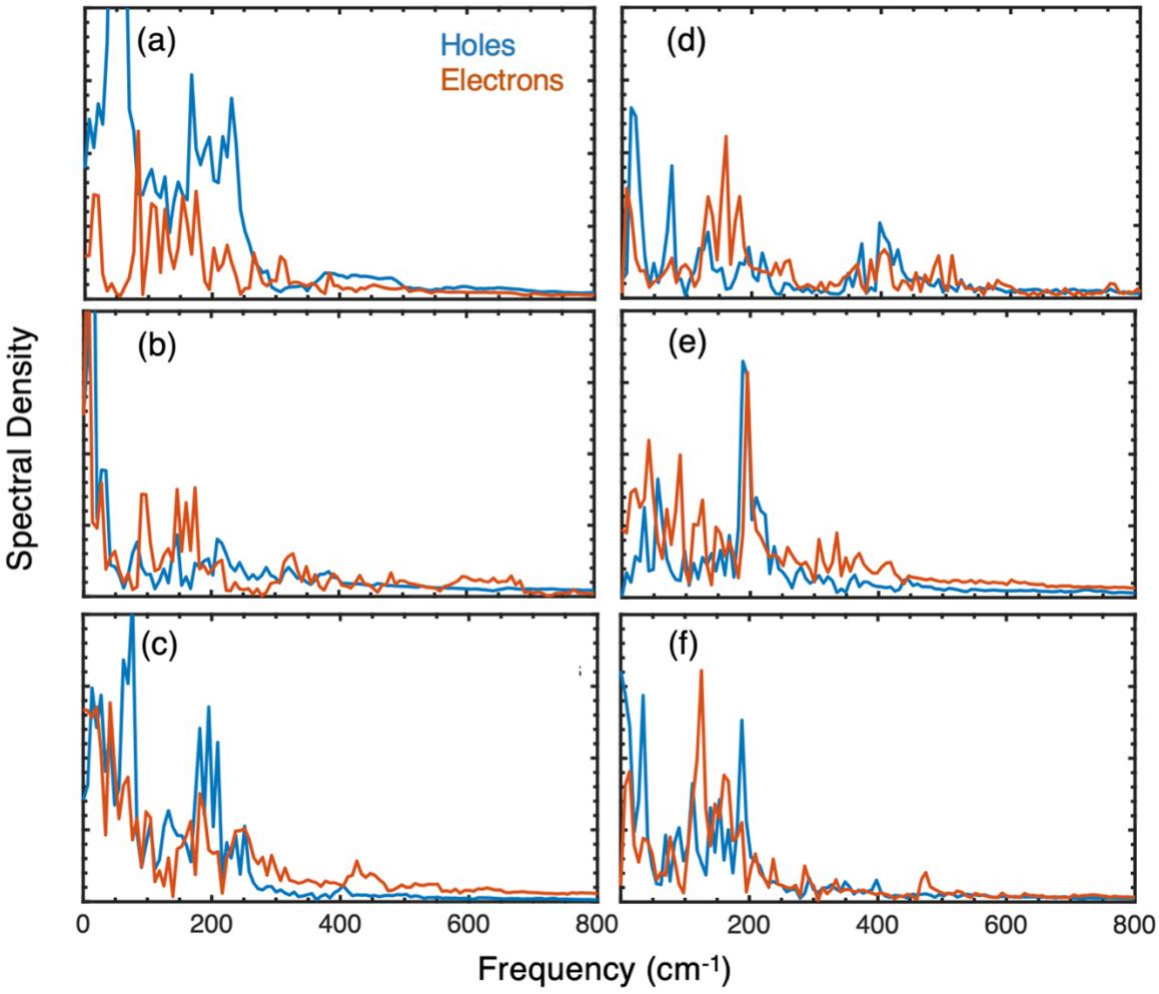

Figure S11. The phonon influence spectra obtained by computing the Fourier transform of the autocorrelation function of energy gaps between orbital corresponding to HOMO and orbital 1 eV lower in energy, marked as holes in blue, and the energy gaps between orbital corresponding to LUMO and KS orbital 1 eV higher in energy, marked as electrons in orange. The spectral density units are arbitrary, but same scaling is adapted for comparison among all nanostructures. a) $Cd_{33}Se_{33}$, (b) $Cd_{28}Se_{17}F_{22}$, (c) $Cd_{28}Se_{17}Cl_{22}$, (d) $Cd_{17}Se_{28}H_{22}$, (e) $Cd_{17}Se_{28}Na_{22}$ and (f) $Cd_{17}Se_{28}K_{22}$ quantum dots.

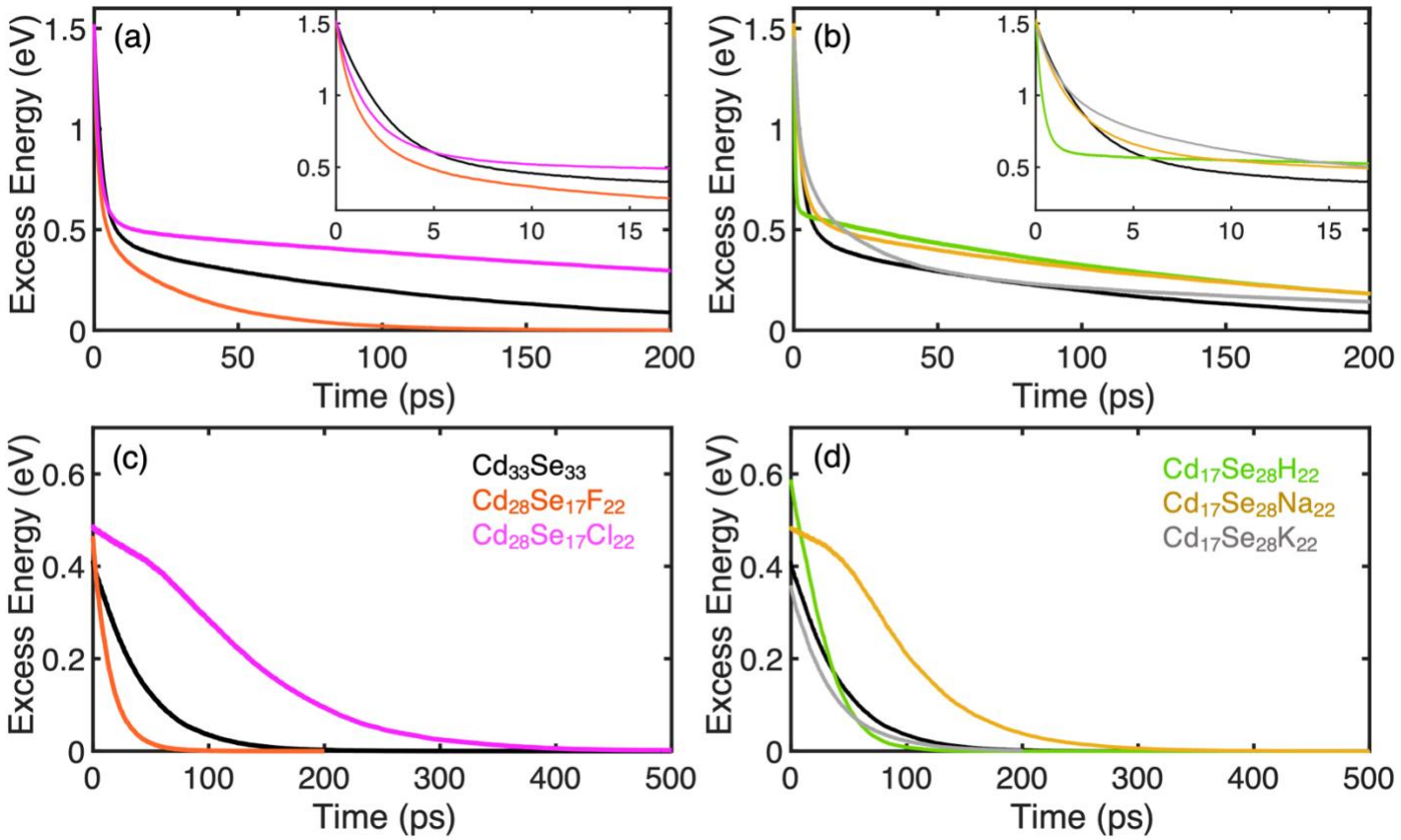

Figure S12. The energy dissipation of electrons starting relaxation at 1.5 eV energy for (a) Cd-rich QDs, (b) Se-rich QDs. The relaxation has two components (fast and slow) of energy dissipation rates. Insets show the zoomed image for fast component. The energy relaxation between the two lowest conduction band states from (LUMO+1) to (LUMO) is displayed in (c) for Cd-rich QDs, and (d) Se-rich QDs.

Table S4. Bader charges averaged over core and surface atoms for all nanoclusters under investigation.

		Cd rich		Se rich		
	$Cd_{33}Se_{33}$	$Cd_{28}Se_{17}F_{22}$	$Cd_{28}Se_{17}Cl_{22}$	$Cd_{17}Se_{28}H_{22}$	$Cd_{17}Se_{28}Na_{22}$	$Cd_{17}Se_{28}K_{22}$
Core	0.50	-1.96	-2.02	2.44	2.72	2.41
Surface	-0.50	1.96	2.02	-2.44	-2.72	-2.41
Ligand	-	-0.72	-0.57	-0.05	0.80	0.80

Table S5. The dephasing time in femtoseconds and root-mean-square (RMS) value of absolute non-adiabatic coupling (NAC) in meV between the LUMO and LUMO+1.

		Cd rich		Se rich		
	$Cd_{33}Se_{33}$	$Cd_{28}Se_{17}F_{22}$	$Cd_{28}Se_{17}Cl_{22}$	$Cd_{17}Se_{28}H_{22}$	$Cd_{17}Se_{28}Na_{22}$	$Cd_{17}Se_{28}K_{22}$
Dephasing time (fs)	10.9	8.0	14.5	16.0	12.9	10.8
RMS NAC (meV)	2.5	4.5	2.2	4.6	2.5	2.5

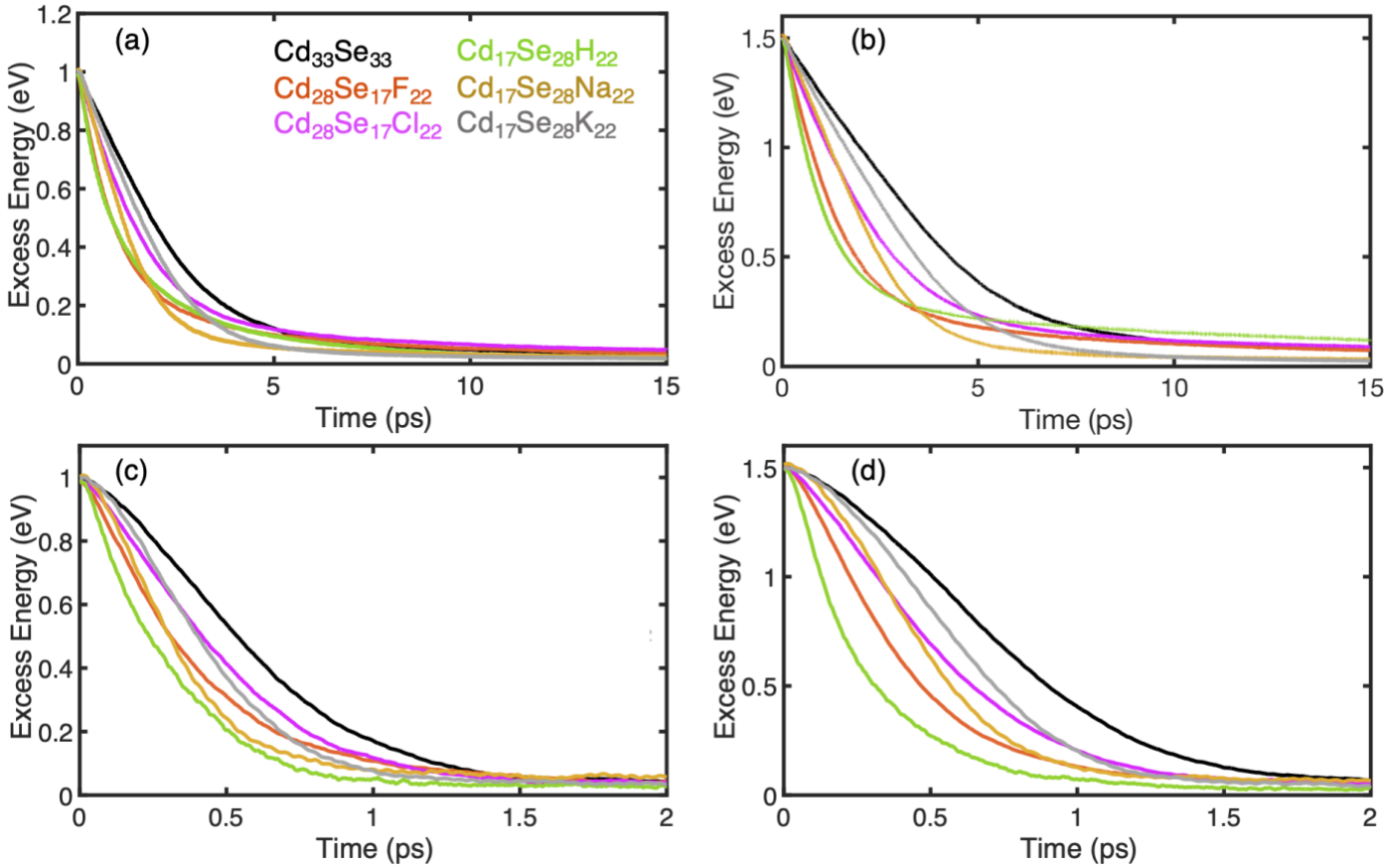

Figure S13. Energy dissipation during the hole relaxation starting at 1 eV (a) and 1.5 eV (b) deep in the VB and using DISH algorithm and FSSH method (c) and (d), respectively. Despite an order of magnitude faster relaxation time for FSSH data compared to DISH, both methods show similar trends in hole relaxation for QDs with heavy ligands. However, systems with F^- and H^+ ligands feature more significant deviations between methods due to larger energy splitting between states at the edge of the VB, which results in the pure dephasing time being shorter than the quantum transition time. Overall, inclusion of the decoherences effect to NAMD is important even for relatively dense hole states.

Table S6. Comparison of slow and fast relaxation time components for all quantum dots under investigation, corresponding to relaxation shown in Figure s4 in main paper.

	Relaxation time (ps)	
	Slow component (τ_1)	Fast component (τ_2)
$Cd_{33}Se_{33}$	76.4	1.3
$Cd_{28}Se_{17}F_{22}$	16.2	1.2
$Cd_{28}Se_{17}Cl_{22}$	162.3	1.3
$Cd_{17}Se_{28}H_{22}$	75.2	0.3
$Cd_{17}Se_{28}Na_{22}$	156.3	1.8
$Cd_{17}Se_{28}K_{22}$	60.0	4.5